Dynamic Control of Cantilever Bistable Composites: Theory and Experiment

Xingping Fan[1] and Jiaying Zhang[1*]

[1] School of Aeronautic Science and Engineering, Beihang University, Beijing 100191, China;

E-mail: jiaying.zhang@buaa.edu.cn

Abstract. Bistable composite laminates, capable of maintaining two stable configurations without continuous energy input, are promising candidates for morphing aerospace structures. This study investigates the nonlinear dynamic behavior of cantilevered bistable composite plates and proposes a resonance-based actuation strategy for efficient configuration switching. A nonlinear dynamic model is developed based on Hamilton's principle and the Rayleigh–Ritz method to accurately model nonlinear dynamic behavior of bistable plates. The dynamic characteristics under varying excitation amplitudes are analyzed through bifurcation diagrams, time histories, phase portraits, and Poincaré maps, revealing the evolution from periodic oscillations to period-doubling bifurcations, chaotic motion, and eventually snap-through. As the excitation frequency approaches the modal frequency, the vibration amplitude increases significantly. When the excitation amplitude exceeds a critical threshold, snap-through occurs, accompanied by the structure switching from one stable state to another. The theoretical predictions show good agreement with the experimental observations. The proposed resonance-based strategy enables rapid and energy-efficient configuration switching, providing practical insights for morphing structure design.

Keywords: Bistability; Clamped boundary condition; Dynamic snap-through behaviors; Chaotic vibrations; vibration experiment

1.Introduction

In modern aerospace engineering, the primary objectives are structural lightweighting and energy efficiency. Aircrafts are supposed to maintain superior aerodynamic performance under diverse and rapidly changing flight conditions, which often involve conflicting requirements such as maneuverability, range, and payload capacity. Conventional fixed-wing and rigid rotor designs are usually optimized for specific operating conditions, resulting in significant performance degradation in off-design environments. To overcome this limitation, morphing technologies have been proposed. These technologies enable aircraft to actively change their aerodynamic shapes to adapt to different flight environments (Molinari et al., 2016; Reich and Sanders, 2007; Stanewsky, 2000). Compared to traditional mechanical structures, smart adaptive structures offer numerous advantages: active shape control not only reduces drag, improves lift-to-drag ratio, and enhances overall aerodynamic efficiency, but also integrates functionalities into load-bearing components, which reducing mechanical complexity and system weight. For example, Daynes et al. (2011) realized multistability in composite intakes by optimizing prestress and bending stiffness; Kim et al. (2010) designed a bio-inspired Venus flytrap robot using bistable asymmetric CFRP structures and SMA springs to attain rapid closure; Daynes et al. (2010) introduced bistable trailing-edge flaps into a full-scale helicopter rotor section, enabling stable shape switching with low actuation energy; Diaconu et al. (2008) explored the potential application of asymmetric bistable laminates for morphing wing sections; Zhang et al. (2019) investigated the nonlinear dynamic characteristics of an SMA-wire-actuated bistable beam through a simplified spring–mass model, and demonstrated that the model can accurately predict various dynamic behaviors.

Bistable composite laminates have gained significant attention for their application in morphing wings and adaptive structures due to their intrinsic multistability and superior mechanical performance (Arrieta et al., 2009; Barbarino et al., 2011; Daynes et al., 2010; Nicassio et al., 2018). They are capable of maintaining two stable shapes without continuous energy input and can rapidly switch configurations via snap-through once external loading exceeds a critical threshold. Since Hyer (1981) first demonstrated the bistability of asymmetric laminates, research has broadened from investigating curvature induced by

residual stresses and the underlying mechanism of bistability (Dano and Hyer, 1998; Dano and Hyer, 2002) to analytical modeling, finite element simulations, and experimental validations (Brampton et al., 2013; Mattioni et al., 2009; Mattioni et al., 2008). Recently, some works focus on nonlinear dynamic responses under external excitation, which includes periodic oscillations, period-doubling bifurcations, quasi-periodic motions, and chaos. Utilizing reduced-order models, energy methods, and multi-mode Galerkin approximations, researchers have revealed the coexistence of stable and unstable branches, providing a theoretical basis for engineering applications. For instance, Potter et al. (2007) experimentally observed snap-through transitions of [0/90] asymmetric bistable laminates; Pirrera et al. (2010) developed a higher-order polynomial theoretical model to track equilibrium states with varying control parameters, identifying both stable and unstable configurations as well as bifurcation points; Arrieta et al. (2011) investigated the geometrical and nonlinear behavior of bistable cylindrical plates; and Wu et al. (2020) proposed a modified theoretical model to describe stable configurations, bifurcation phenomena, and snap-through of bistable laminates. In addition, Zheng et al. (2021) reported jump-induced chaotic oscillations and metastable chaos in asymmetric bistable laminates under combined external and parametric excitations.

Many studies have built on these theoretical foundations of bistable structures by exploring the geometric and stiffness variations for morphing applications. Betts et al. (2012) proposed an optimization method for asymmetric bistable laminates, which aim to maximize bending stiffness along the loading direction while minimizing stiffness in the snap-through direction. This approach allows to achieve large deflections beyond conventional cross-ply designs. Arrieta et al. (2013) and Bilgen et al. (2013) modeled the aeroelastic response of bistable wing-shaped laminates and further proposed passive load alleviation concepts (Arrieta et al., 2012; Arrieta et al., 2014). Kuder et al. (2016) examined the aero-structural coupling of variable stiffness bistable laminates, optimizing their placement and properties within airfoils to maximize compliance selectivity. Boddapati and Arrieta (2021) developed a low-aspect-ratio slotted bistable laminate and validated its effectiveness as a morphing trailing-edge device through wind tunnel experiments .(Boddapati et al., 2023)

To improve the efficiency of configuration switching in bistable laminates and enhance morphing performance, resonance-based actuation has been introduced. By tuning the excitation frequency close to structural resonances, this approach amplifies responses while reducing significant input or energy consumption. For example, Kakogawa et al. (2018) developed a serpentine robot with parallel elastic actuators, achieving a 72% reduction in energy consumption through resonance; Kim et al. (2008) designed a resonant trailing-edge flap system for helicopter rotors and a nonlinear piezoelectric buckled beam amplifier, attaining high-gain actuation while avoiding undesired snap-through and chaotic responses; Bolsman et al. (2009) designed a resonant actuation mechanism for a flapping MAV, enhancing wing root rotation and reducing power demands; Zhang et al. (2022) proposed a resonant passive energy balancing strategy for morphing helicopter blades, in which a negative stiffness mechanism is employed to tailor the natural frequency and reduce actuation effort, enabling efficient dynamic morphing through resonance. Taghipour et al. (2022) extended this resonant concept by analyzing blades with bend–twist coupling, revealing that both structural coupling and aerodynamic parameters are critical for controlling pitch dynamics. Yao et al. (2024) developed a pre-twisted blade model using a Ti–SiC fiber-reinforced composite with a NACA airfoil. They investigated how rotational speed, aspect ratio, and pre-twist angle influence vibration characteristics, providing insights into blade energy efficiency. In parallel, nonlinear passive control mechanisms have been proposed to enhance dynamic stability of flexible aerospace structures. Wang et al. (2025b) applied a nonlinear energy sink to suppress flutter in variable-thickness porous sandwich conical shells under combined aerodynamic and thermal loads, providing optimized vibration control solutions.

However, a significant challenge remains: when integrated into morphing aircraft systems, bistable structures may lose their multistability due to imposed boundary conditions, which can lead to structural failure (Sanders et al., 2003). Although these laminates exhibit remarkable versatility, the coupling effects of boundary conditions can greatly influence bistability(Schioler and Pellegrino, 2008). Therefore, it is crucial to consider the impact of boundary conditions during design, optimization, and manufacturing to maintain their unique

properties within complete systems. Different boundary conditions have been investigated, including clamped, simply supported, and cantilever cases (Liu et al., 2026; Liu et al., 2023; Wang et al., 2025a; Wu et al., 2021; Zhang et al., 2025) Among these, bistable structures with cantilever boundaries are particularly suitable for morphing wing applications. While most existing studies have focused on characterizing multistability and nonlinear vibration behaviors under such conditions (Boddapati et al., 2024; Brunetti et al., 2020; Brunetti et al., 2018a; Brunetti et al., 2022; Brunetti et al., 2018b; Brunetti et al., 2016), efficient actuation strategies for configuration switching remain insufficiently explored.

Despite extensive research on bistable laminates and nonlinear vibration, the dynamic snap-through behavior of cantilevered bistable composite laminates under resonance excitation has not been systematically investigated. In particular, the transition mechanisms from periodic motion to chaos and ultimately to snap-through, as well as their experimental validation under practical cantilever boundary conditions, remain insufficiently understood. A comprehensive understanding of these resonance-induced transition mechanisms is essential for developing efficient and controllable morphing strategies in adaptive structures.

This study investigates the nonlinear dynamic response of cantilevered bistable composite laminates and proposes a resonance-based control strategy to achieve rapid and controllable configuration transitions. A dynamic model of cantilevered bistable composite laminates is developed based on Hamilton's principle to accurately capture the complex dynamic behavior of the system. Dynamic properties of the system under various external excitations are systematically analyzed through amplitude-frequency response curves, bifurcation diagrams, time histories, phase portraits, and Poincaré maps. Numerical results are further validated by experiments. The paper is organized as follows. Section 2 introduces the concept of resonance-based actuation through a simplified nonlinear spring–mass model. Section 3 establishes the dynamic model of the cantilever bistable laminates. Section 4 introduces the experimental setup and testing method. Section 5 systematically investigates the nonlinear dynamics of the cantilever bistable laminates through the analytical model. Section 6 validates the analytical results through vibration experiments. Section 7 proposed a

resonance-based actuation strategy to achieve efficient configuration switching. Section 8 concludes the key conclusions of this study.

2. Resonance-Based Actuation in Nonlinear Oscillators

To clearly illustrate the concept of resonance-based actuation and its advantages, this section begins by considering a classical mass-spring-damper system. This system includes a nonlinear stiffness term up to the fifth order, thereby coupling inertia, damping, and nonlinearity in their simplest form. Analyzing this simplified model reveals the relationship between input energy and excitation frequency, showing how frequency tuning near resonance can significantly reduce the actuation energy required to achieve a desired response. The insights gained from this elementary system provide the theoretical foundation for the dynamic analysis and control strategy design of the more complex cantilevered bistable laminates presented in the subsequent sections.

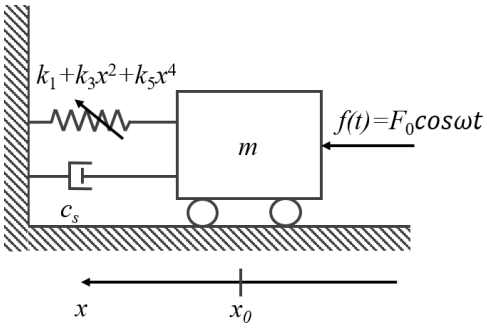

Figure 1. Simplified nonlinear mass–spring–damper model with a single degree of freedom.

The equation of motion is:

$$m\ddot{x} + c_s\dot{x} + k_1x + k_3x^3 + k_5x^5 = f(t) \tag{1}$$

Here, $f(t)$ denotes the excitation force provided by the actuator, while m, c_s, k_1, k_3 and k_5 represent the mass, damping coefficient, and linear, cubic, and quintic stiffness coefficients, respectively. To ensure the symmetry of the system's nonlinear stiffness, the coefficients of the quadratic and quartic terms are set to zero. For simplicity, the motion of the mass is prescribed to be:

$$x(t) = X\cos(\omega t) \tag{2}$$

where ω is the motion frequency. Substituting Eq. (2) into Eq. (1) yields:

$$\begin{aligned} f(t) = &\left(-mX\omega^2 + k_1X + \frac{3}{4}k_3X^3 + \frac{5}{8}k_5X^5\right)\cos(\omega t) \\ &-c_sX\omega\sin(\omega t) \\ &+\left(\frac{1}{4}k_3X^3 + \frac{5}{16}k_5X^5\right)\cos(3\omega t) + \frac{1}{16}k_5X^5\cos(5\omega t) \end{aligned} \tag{3}$$

The instantaneous power input to the system is defined as:

$$p_i = f\dot{x} \tag{4}$$

Substituting Eqs. (2) and (3) yields the instantaneous power expression:

$$\begin{aligned} p_i(t) = &\frac{c_s\omega^2X^2}{2} - \frac{c_s\omega^2X^2}{2}\cos(2\omega t) \\ &+\left[\frac{\omega X^2}{2}\left(m\omega^2 - k_1 - \frac{3}{4}k_3X^2 - \frac{5}{8}k_5X^4\right) + \frac{\omega k_3X^4}{8} + \frac{5\omega k_5X^6}{32}\right]\sin(2\omega t) \\ &-\left(\frac{\omega k_3X^4}{8} + \frac{5\omega k_5X^6}{32} - \frac{\omega k_5X^6}{32}\right)\sin(4\omega t) \\ &-\frac{\omega k_5X^6}{32}\sin(6\omega t) \end{aligned} \tag{5}$$

The average power input can be obtained from the work per cycle:

$$\bar{p_i} = \frac{\omega}{2\pi}W_0 \tag{6}$$

Where W_0 is the work per actuation cycle:

$$W_0 = \oint f dx = \int_0^T f\dot{x}dt = \int_0^T p_i dt \tag{7}$$

and $T = 2\pi/\omega$ is the driving period. Substituting Eq. (5) into Eq. (7) and simplifying gives:

$$W_0 = \pi c_s\omega X^2 \tag{8}$$

Critically, this result demonstrates that the nonlinear stiffness terms do not contribute to the average power consumption. However, this conclusion overlooks a key practical limitation: most actuators are non-regenerative. When p_i is negative, they cannot absorb or store energy but merely dissipate it. Thus, Eq. (8) represents the minimum possible work per cycle. To establish a more practical and realistic metric, we define the Positive Instantaneous Power (PIP) function, p_+ which sets all negative power instances to zero, acknowledging that energy cannot be recovered during these intervals:

$$p_+ = \begin{cases} p_i, & p_i > 0 \\ 0, & p_i \leq 0 \end{cases} \tag{9}$$

The corresponding positive work per cycle is then:

$$W_+ = \int_0^T p_+ dt \tag{10}$$

An approximate analytical solution for W_+ can be derived by neglecting higher harmonics (4ω and 6ω terms) in Eq. (5) and time-shifting the resulting expression to the form $p_i = P\cos 2\omega t + P_0$. Exploiting symmetry and periodicity, the positive work is then:

$$W_+ \approx 4\int_0^{t^*} p_i dt = 2\left(\frac{P}{\omega}\sin(2\omega t^*) + 2P_0 t^*\right) \tag{11}$$

where

$$\begin{aligned} \mathrm{P} &= \frac{\omega X^2}{2}\sqrt{\left(-\omega^2 m + k_1 + \frac{3}{4}k_3 X^2 + \frac{5}{8}k_5 X^4\right)^2 + (c_s\omega)^2 P_0} \\ &= \frac{c_s \omega^2 X^2}{2} \end{aligned} \tag{12}$$

and t^* is the time from the peak instantaneous power to its first zero-crossing (or to the minimum if no zero-crossing exists within the half-period):

$$t^* = \begin{cases} \dfrac{\cos^{-1}\left(-\frac{P_0}{P}\right)}{2\omega}, & P > P_0 \\ \dfrac{\pi}{2\omega}, & P \leq P_0 \end{cases} \tag{13}$$

For a specific case study, consider a non-dimensional system with parameters chosen such that the equivalent linear stiffness is unity, placing the system at a resonant condition. We set $m = X = 1$, $k_1 = 0.1$, $k_3 = 0.2$, $k_5 = 0.5$, and $c_s = 0.2$. The condition for equivalent linear stiffness is derived from setting the coefficient of the fundamental harmonic in Eq. (3) to zero, excluding damping:

$$-\omega_0^2 m + k_1 + \frac{3}{4}k_3 X^2 + \frac{5}{8}k_5 X^4 = 0 \tag{14}$$

With the chosen parameters and satisfying Eq. (14), the resonant frequency is $\omega = 0.75$. As shown in Figure 2, driving the system at or near this resonant frequency significantly reduces

the positive work W_+ compared to off-resonant excitation, leading to substantial energy savings.

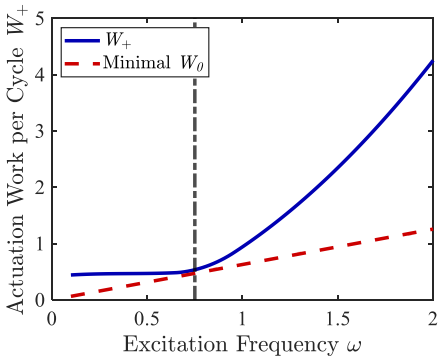

Figure 2. Comparison of the work per cycle for a dimensionless linear system at different frequencies with the theoretically predicted minimum work per cycle.

To explore the forced response sensitivity of the nonlinear system, we consider:

$$m\ddot{x} + c_s\dot{x} + k_1x + k_3x^3 + k_5x^5 = \mathrm{F}\cos\omega_0 t \tag{15}$$

Assuming a steady-state response $x(t) = X\cos(\omega_0 t+\varphi)$ and applying the harmonic balance method yields the amplitude-frequency relationship:

$$\left[\left(k_1 - m\omega_0^2 + \frac{3}{4}k_3X^2 + \frac{5}{8}k_5X^4\right)^2 + (c_s\omega_0)^2\right]X^2 = F^2 \tag{16}$$

Figure 3(a) depicts the variation of the response amplitude X with the excitation frequency under a fixed excitation amplitude. When $\omega \leq 0.48$, the system exhibits no unstable solutions in its frequency response. Figure 3(b) shows the dependence of the response amplitude X on the excitation amplitude F at a fixed excitation frequency. It is evident that at $\omega = 0.48$, the system maintains a single stable equilibrium regardless of the increase in F, indicating that snap-through cannot be triggered.

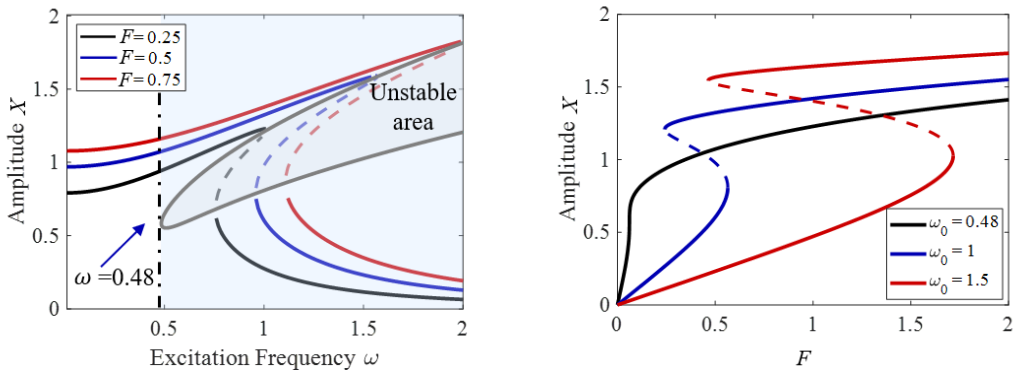

(a) (b)

Figure 3. System response amplitude under external excitation: (a) amplitude-frequency curves; (b) amplitude–force curves.

These results confirm that the snap-through phenomenon occurs within a specific frequency range. Outside of this range, the lack of unstable branches in the frequency response means that snap-through does not happen at any practically attainable excitation level. This phenomenon highlights the crucial role of frequency selection in exploiting nonlinear dynamic responses and provides a strong reason for optimizing the driving frequency in the subsequent analysis of cantilevered bistable plates.

Based on the understanding of resonance-driven actuation in nonlinear systems gained from this simplified analysis, a comprehensive dynamic model of the cantilevered bistable laminate is established, and the effectiveness of this resonance strategy is validated in the following sections.

3. Theoretical Modeling of Cantilever Bistable Composite Laminates

3.1. Stable Configurations and Material Parameters

Cured cross-ply bistable composite laminates have two stable configurations and one unstable configuration, which resulting from residual thermal stresses developed during the manufacturing process. In this study, the two stable states of the cantilevered bistable laminate are considered, which is illustrated in Figure 4. The cantilever boundary condition is achieved by fully clamping one short edge of the laminate, while the other three edges are left free, thereby representing typical engineering configurations such as morphing wing flaps. The

shaker, rigidly attached to the clamp, provides harmonic base excitation normal to the plate surface, inducing oscillations in the plate.

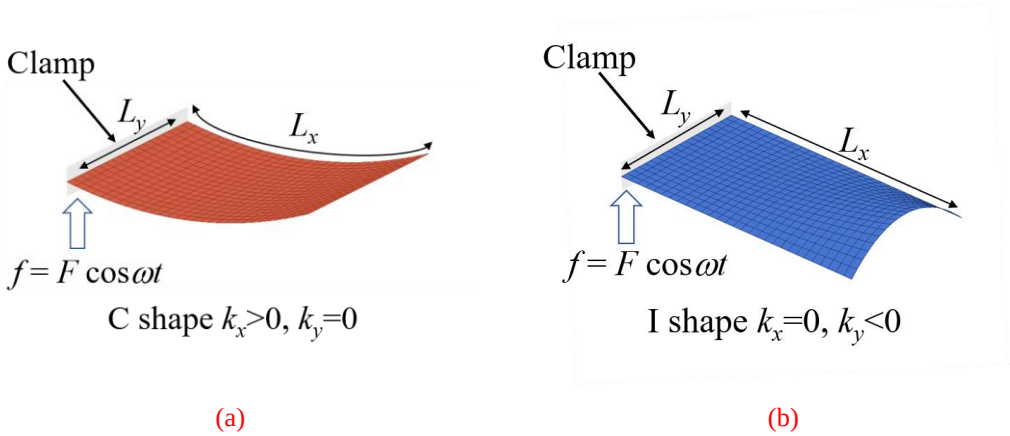

(a) (b)

Figure 4. Two stable configurations of a bistable cantilever plate, (a)C Shape, (b)I Shape.

The laminate is a symmetric cross-ply [0/90] configuration with total thickness h, length L_x and width L_y. This layup is commonly adopted due to its notable bistability and ease of manufacturing. Figure 5 illustrated the cantilever boundary condition and the sequence of [0/90] layup.

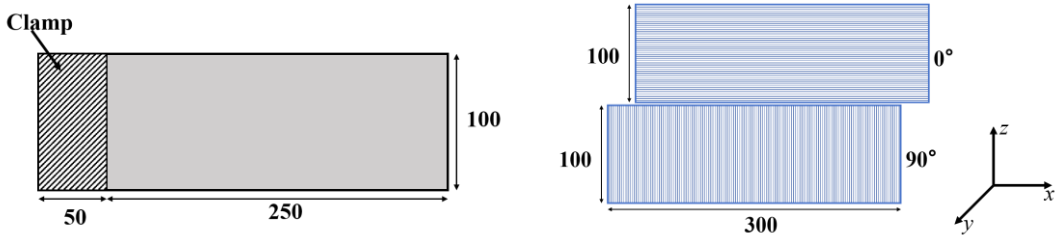

(a) (b)

Figure 5. Schematic of the bistable structure, (a) cantilever boundary, (b) [0/90] laminate layup.

Table 1. Material parameters are given for the asymmetric bi-stable composite laminates.

parameter	value	parameter	value
E_1	124.9GPa	α_1	-0.1×10^{-6}℃$^{-1}$
E_2	7.9GPa	α_2	2×10^{-5}℃$^{-1}$
G_{12}	5.6GPa	L_x	300mm
G_{13}	5.6GPa	L_y	100mm
G_{23}	5.6GPa	h_0	0.15mm
v	0.3	/	/

The cured curvature of the laminate, which is the source of its bistability, primarily results from the mismatch in the coefficients of thermal expansion between the 0° and 90° plies during cooling process after curing. The key geometric and material parameters used in this study are summarized in Table 1.

3.2. Governing Equations Based on Hamilton's Principle

The analytical model is developed under the following assumptions: the bistable rectangular plate is initially flat upon manufacture before being cooled to room temperature, and the laminate is under a cantilever boundary condition. A dynamic model for the orthotropic bistable composite laminate is formulated via Hamilton's principle, which states that the time integral of the system's Lagrangian is stationary:

$$\int_{t_1}^{t_2} \delta(T(t)) + W_F(t) - \Pi(t))dt = 0 \tag{17}$$

Here, $T(t)$ is the kinetic energy, $W_F(t)$ is the virtual work done by external forces, and $\prod(t)$ is the total potential energy.

Given that the plate thickness is significantly smaller than its in-plane dimensions, the Kirchhoff hypothesis are adopted here. The in-plane strain at any point through the thickness is:

$$\begin{bmatrix} \varepsilon_x \\ \varepsilon_y \\ \gamma_{xy} \end{bmatrix} = \begin{bmatrix} \varepsilon_x^0 \\ \varepsilon_y^0 \\ \gamma_{xy}^0 \end{bmatrix} + z \begin{bmatrix} k_x \\ k_y \\ k_{xy} \end{bmatrix} \tag{18}$$

where the curvature vector $\boldsymbol{k}$ is defined as:

$$\boldsymbol{k} = \begin{bmatrix} k_x \\ k_y \\ k_{xy} \end{bmatrix} = \begin{bmatrix} -\dfrac{\partial^2 w}{\partial x^2} \\ -\dfrac{\partial^2 w}{\partial y^2} \\ -2\dfrac{\partial^2 w}{\partial x \partial y} \end{bmatrix} \tag{19}$$

Here, ε_x^0, ε_y^0 and γ_{xy}^0 are the mid-plane strains of the laminated plate.

(Hyer, 1981) pointed out that in order to account for the large deformations of bistable laminated plates, nonlinear terms must be included in the geometric equations. According to

the von Kármán assumptions, the relationship between the mid-plane strains and displacements of the bistable laminated plate is given by:

$$\boldsymbol{\varepsilon}^0 = \begin{bmatrix} \varepsilon_x^0 \\ \varepsilon_y^0 \\ \gamma_{xy}^0 \end{bmatrix} = \begin{bmatrix} \dfrac{\partial u^0}{\partial x} + \dfrac{1}{2}\left(\dfrac{\partial w}{\partial x}\right)^2 \\ \dfrac{\partial v^0}{\partial y} + \dfrac{1}{2}\left(\dfrac{\partial w}{\partial y}\right)^2 \\ \dfrac{\partial u^0}{\partial y} + \dfrac{\partial v^0}{\partial x} + \dfrac{\partial w}{\partial x}\dfrac{\partial w}{\partial y} \end{bmatrix} \tag{20}$$

In the above expressions u^0, v^0 and w represent the in-plane displacements and the out-of-plane displacement, respectively.

The total elastic potential energy, accounting for residual thermal stresses from the curing process and assuming no external energy input during curing, is:

$$\Pi = \frac{1}{2}\int_V [(\sigma_x - \sigma_x^T)\varepsilon_x + (\sigma_y - \sigma_y^T)\varepsilon_y + (\sigma_{xy} - \sigma_{xy}^T)\varepsilon_{xy}]dV \tag{21}$$

where σ and ε are the stress and strain tensors of the laminate, respectively, σ^T and ε^T are the thermally induced stress and strain, which are given by:

$$\begin{aligned} \sigma_x &= \bar{Q}_{11}\varepsilon_x + \bar{Q}_{12}\varepsilon_y + \bar{Q}_{16}\gamma_{xy} \\ \sigma_y &= \bar{Q}_{12}\varepsilon_x + \bar{Q}_{22}\varepsilon_y + \bar{Q}_{26}\gamma_{xy} \\ \sigma_{xy} &= \bar{Q}_{16}\varepsilon_x + \bar{Q}_{26}\varepsilon_y + \bar{Q}_{66}\gamma_{xy} \end{aligned} \tag{22}$$

$$\begin{aligned} \sigma_x^T &= \bar{Q}_{11}\varepsilon_x^T + \bar{Q}_{12}\varepsilon_y^T + \bar{Q}_{16}\gamma_{xy}^T \\ \sigma_y^T &= \bar{Q}_{12}\varepsilon_x^T + \bar{Q}_{22}\varepsilon_y^T + \bar{Q}_{26}\gamma_{xy}^T \\ \sigma_{xy}^T &= \bar{Q}_{16}\varepsilon_x^T + \bar{Q}_{26}\varepsilon_y^T + \bar{Q}_{66}\gamma_{xy}^T \end{aligned} \tag{23}$$

$\bar{\boldsymbol{Q}}$ is the reduced stiffness term of the laminate, which is calculated according to the following equation:

$$\begin{bmatrix} \bar{Q}_{11} \\ \bar{Q}_{12} \\ \bar{Q}_{22} \\ \bar{Q}_{16} \\ \bar{Q}_{26} \\ \bar{Q}_{66} \end{bmatrix} = \begin{bmatrix} C^4 & 2C^2S^2 & S^4 & 4C^2S^2 \\ C^2S^2 & C^4 + S^4 & C^2S^2 & -4C^2S^2 \\ S^4 & 2C^2S^2 & C^4 & 4C^2S^2 \\ C^3S & CS^3 - C^3S & -CS^3 & -2CS(C^2 - S^2) \\ CS^3 & C^3S - CS^3 & -C^3S & 2CS(C^2 - S^2) \\ C^2S^2 & -2C^2S^2 & C^2S^2 & (C^2 - S^2)^2 \end{bmatrix} \begin{bmatrix} Q_{11} \\ Q_{12} \\ Q_{22} \\ Q_{66} \end{bmatrix} \tag{24}$$

where $C = \cos\beta$, $S = \sin\beta$. The relationship between $\boldsymbol{Q}$ and the engineering elastic constants of a single layer is as follows:

$$\begin{cases} Q_{11} = \dfrac{E_1}{1-\nu_{12}\nu_{21}} \\ Q_{12} = \dfrac{\nu_{12}E_2}{1-\nu_{12}\nu_{21}} \\ Q_{22} = \dfrac{E_2}{1-\nu_{12}\nu_{21}} \\ Q_{66} = G_{12} \end{cases} \tag{25}$$

Due to the nonzero coupling stiffness matrix of the asymmetric laminate, there exists a bending–stretching coupling effect between the laminate layers. The thermally induced strain depends on the curing temperature:

$$\begin{aligned} \varepsilon_x^T &= \alpha_x \Delta T \\ \varepsilon_y^T &= \alpha_y \Delta T \\ \gamma_{xy}^T &= \alpha_{xy} \Delta T \end{aligned} \tag{26}$$

ΔT is the temperature difference in the cooling process, where α_x, α_y, α_{xy} are the thermal expansion coefficients, which can be expressed as:

$$\begin{cases} \alpha_x = \alpha_1\cos^2\beta + \alpha_2\sin^2\beta \\ \alpha_y = \alpha_1\sin^2\beta + \alpha_2\cos^2\beta \\ \alpha_{xy} = (\alpha_1 - \alpha_2)\sin\beta\cos\beta \end{cases} \tag{27}$$

β is the laying angle of the single-layer prepreg board.

When the bending curvature is assumed to be constant, the theoretical model does not accurately predict the stiffness of the laminate. Therefore, this study assumed that the bending curvature of the laminate is not constant. Considering the boundary conditions of the laminate as well as the symmetric and antisymmetric characteristics of its deformation, the out-of-plane displacement is assumed to follow a fourth-order polynomial form:

$$\begin{aligned} w(x,y) &= \sum_{q=1}^{n}\sum_{r=1}^{n} a_i x^q y^r, (n = 4, i = 1,2,3\ldots) \\ u(x,y) &= \sum_{q=1}^{n}\sum_{r=1}^{n} b_i x^q y^r, (n = 4, i = 1,2,3\ldots) \end{aligned} \tag{28}$$

$$v(x,y)=\sum_{q=1}^{n}\sum_{r=1}^{n}c_i x^q y^r,(n=4,i=1,2,3\ldots)$$

To balance accuracy and computational efficiency, a convergence study on the polynomial order of the displacement function was conducted. Cubic, quartic, and quintic polynomial approximations were evaluated by comparing their predictions of the central deflection in the C stable configuration. The results show that the cubic assumption leads to noticeable deviations, whereas the improvement from fourth to fifth order is marginal (less than 2%) but accompanied by a significant increase in nonlinear coupling terms and computational complexity. Therefore, the fourth-order polynomial is adopted as an efficient and sufficiently accurate choice.

The boundary conditions that must be satisfied are as follows:

$$\begin{gathered}u(0,y)=0\\ v(0,y)=0\\ w(0,y)=0\\ \frac{\partial w}{\partial x}(0,y)=0\\ \frac{\partial w}{\partial y}(0,y)=0\\ \frac{\partial^2 w}{\partial x^2}(L_x,y)=0\\ \frac{\partial^2 w}{\partial y^2}(L_x,y)=0\\ \frac{\partial^3 w}{\partial x^3}(L_x,y)=0\\ \frac{\partial^3 w}{\partial y^3}(L_x,y)=0\end{gathered}\tag{29}$$

The kinetic energy of the bistable laminated plate is expressed as:

$$T=\frac{1}{2}\int_{\mathrm{V}}\rho_L(\dot{u}^2+\dot{v}^2+\dot{w}^2)dV\tag{30}$$

Based on Hamilton's principle, the Lagrange equation (17), and the assumed displacement functions, the equations of motion of the system are derived as follows:

$$\boldsymbol{M}_1\ddot{\boldsymbol{X}}_1+\boldsymbol{D}(\dot{\boldsymbol{X}}_1)+\boldsymbol{K}_1(\boldsymbol{X}_1)=\boldsymbol{F}_1\tag{31}$$

Here, $\boldsymbol{M}_1$ is the mass matrix, $\boldsymbol{D}(\dot{\boldsymbol{X}}_1)$ is the damping force, and $\boldsymbol{K}_1(\boldsymbol{X}_1)$ represents the nonlinear elastic force. $\boldsymbol{F}_1$ is the external excitation force, which depends on the inertia and acceleration

of the laminated plate. Equation (31) constitutes the governing equation for the nonlinear dynamic analyses presented herein. Direct numerical integration is performed to retain the full nonlinear characteristics of the cantilevered bistable laminate, including geometric nonlinearity, bending–stretching coupling, and residual thermal stresses. This framework enables accurate characterization of the dynamic evolution from periodic oscillations to period-doubling bifurcations, chaotic responses, and snap-through. The numerical solutions serve as the basis for the bifurcation diagrams, time histories, phase portraits, and Poincaré maps presented in Section 5.

4. Experimental Setup and Measurement Methodology

In this section, the experimental setup and testing method are introduced to study the nonlinear dynamics of the bistable cantilever laminates under external excitation. To ensure the accuracy of the dynamic analysis, it is essential to define the geometric parameters of the laminates. The maximum plate length was set to 300 mm due to the constraints of the experimental platform (e.g., shaker and fixtures). Additionally, bistability is highly sensitive to aspect ratio and geometry; extreme dimensions may weaken it (Pirrera et al., 2010). Thus, four dimensions were selected: 300×100 mm, 250×100 mm, 200×100 mm, and 200×80 mm, covering aspect ratios of 2–3 to systematically investigate dimensional effects on the dynamic performance. The specimens are arranged from left to right as shown in Figure 6.

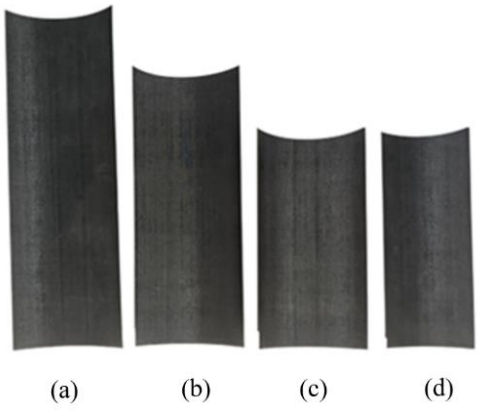

Figure 6. Bistable composite laminated plates of different dimensions, (a)300× 100 mm, (b)250 × 100 mm, (c)200 × 100 mm, (d) 200 × 80 mm.

The vibration experimental setup is shown in Figure 7. The vibration controller (SPIDER-81) generates acceleration excitation signals with varying frequencies and amplitudes. These signals are amplified by a signal amplifier (YE5872A) and applied to the specimens via a shaker (SA-JZ005). A laser displacement sensor (HG-C1100) simultaneously measures the dynamic displacement at a specific point on the laminated plate, and the vibration controller records the time histories collected by the sensor. The measurement point is located at the midpoint of the plate, 50 mm from the clamped boundary, as this position ensures that the displacement variation during snap-through remains within the effective measurement range of the displacement sensor.

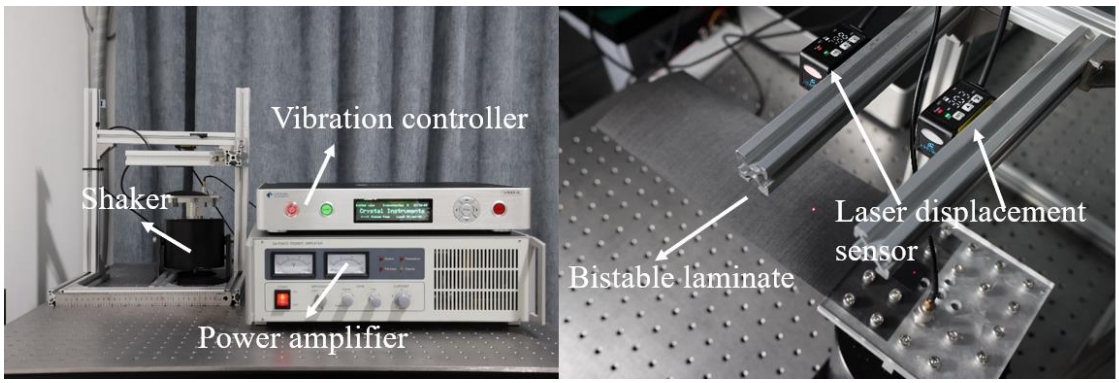

Figure 7. Experimental setup

5. Numerical Analysis of Nonlinear Dynamic Responses

To validate the analytical model for the selected dimensions, it was first employed to predict the two stable shapes of the laminates. Figure 8 illustrates these stable configurations, denoted as C shape and I shape.

To probe the nonlinear dynamics, the system response was characterized using frequency sweeps conducted at a constant rate under a fixed excitation acceleration of 2 m/s². Both forward and backward sweeps were employed, as this method is well-established for identifying nonlinear phenomena. Figure 9-10 presents the frequency response curves for both Configuration I and C, measured over a frequency range of 0 to 20 Hz. These curves effectively elucidate the evolution of the dynamic response.

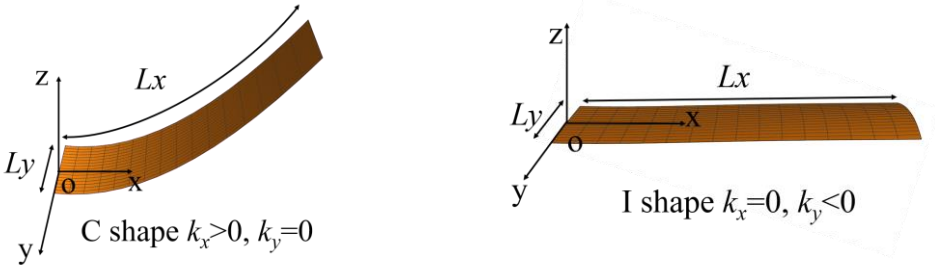

(a) (b)

Figure 8. The two stable configurations predicted by the theoretical model, (a) C Shape, (b) I Shape.

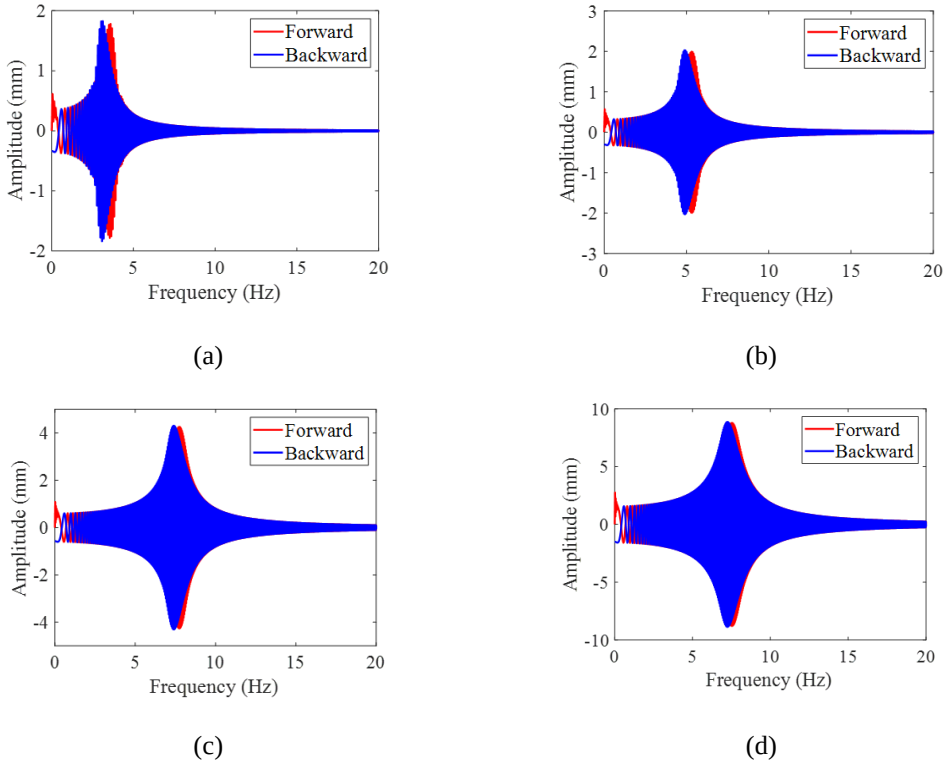

(a) (b)

(c) (d)

Figure 9. Forward and backward frequency sweep results of the C configuration, (a) 300 × 100 mm, (b)250 × 100 mm, (c)200 × 100 mm, (d) 200 × 80 mm.

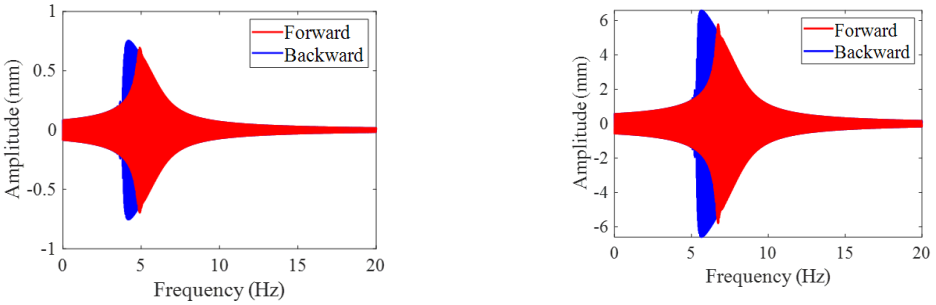

(a) (b)

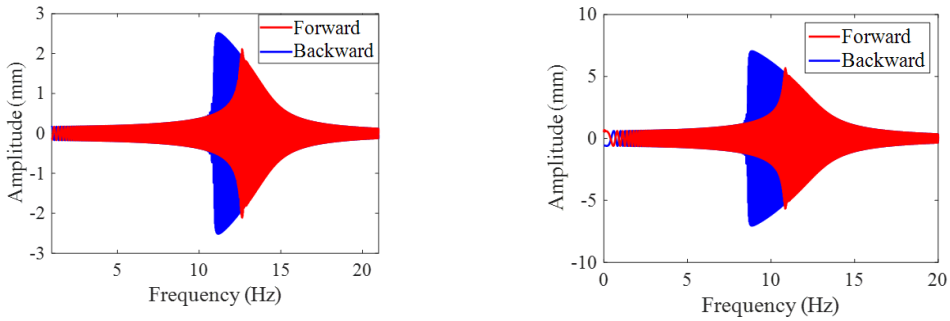

(c) (d)

Figure 10. Forward and backward frequency sweep results of the I configuration, (a) 300 × 100 mm, (b)250 × 100 mm, (c)200 × 100 mm, (d) 200 × 80 mm.

The frequency-sweep analysis reveals typical softening-spring characteristics in the system, with the resonance peak shifting significantly toward lower frequencies. Furthermore, due to the strong nonlinearity of the system, the forward and backward sweep responses do not align. Compared to C shape, I shape exhibits stronger nonlinear responses. This indicates that the degree of nonlinearity in cantilevered bistable composite laminates depends not only on external excitation but is also closely related to their configurations.

Further investigations have been done to examine the periodic and chaotic vibrations of a cantilevered bistable composite laminated plate under various external excitation conditions. Especially on how the system's nonlinear dynamic behavior evolves with increasing excitation amplitude at a fixed excitation frequency. In order to reveal the nonlinear dynamic characteristics, bifurcation diagrams, time histories, phase portraits, and Poincaré maps are employed to identify and classify periodic and chaotic vibrations.

Under the excitation frequency of 7.5 Hz, a bifurcation diagram is plotted based on the displacement coordinate (vertical axis) of the Poincaré mapping points and the excitation amplitude (horizontal axis), which clearly illustrates the evolution of system responses with increasing excitation amplitude. Because the output amplitude of the experimental exciter is limited in the low-frequency range, when the excitation frequency is set to 5 Hz (the resonant frequency of Configuration I), the maximum excitation amplitude of the exciter (6 m/s^2) is insufficient to trigger snap-through of the cantilever bistable plate. The theoretical model also demonstrated that snap-through could not occur under this excitation level. Therefore, 7.5 Hz

is selected as the excitation frequency in subsequent experiments. Although this frequency is slightly higher than the fundamental frequency of Configuration I (5 Hz), it remains within its primary resonance region, allowing the vibration amplitude to be significantly amplified and thereby inducing snap-through at a feasible excitation level. Moreover, after snap-through, the natural frequency of Configuration C is approximately 3.2 Hz, which is far from 7.5 Hz, leading to a rapid decay of vibration amplitude and facilitating stabilization in the new configuration. Thus, the choice of 7.5 Hz effectively leverages the resonance characteristics of the initial stable state while ensuring experimental feasibility.

As shown in Figure 11, the bifurcation diagram clearly displays the transition process of the system under external excitation: as the excitation amplitude gradually increases, the system response evolves from periodic vibration to chaotic motion, and finally undergoes snap-through.

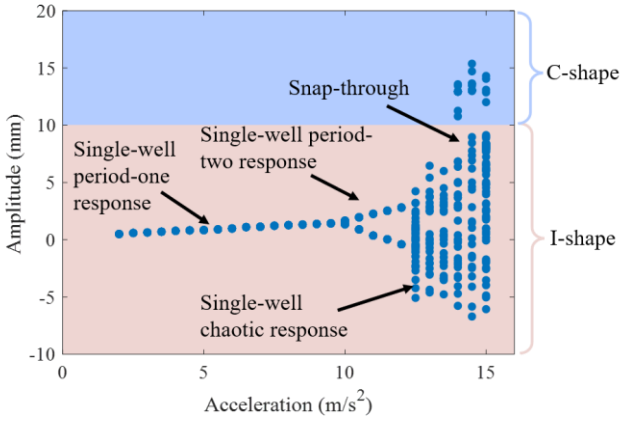

Figure 11. Bifurcation diagram from the analytical model at 7.5 Hz.

At an excitation amplitude of 5 m/s^2, the system exhibits single-period vibration (Fig. 12). The time history (Fig. 12(a)) shows constant amplitude oscillation; the phase portrait and Poincaré map (Fig.12(b)) form a closed trajectory with Poincaré points concentrated at a single location; the amplitude spectrum (Fig.12(c)) displays a peak at the excitation frequency 7.5 Hz.

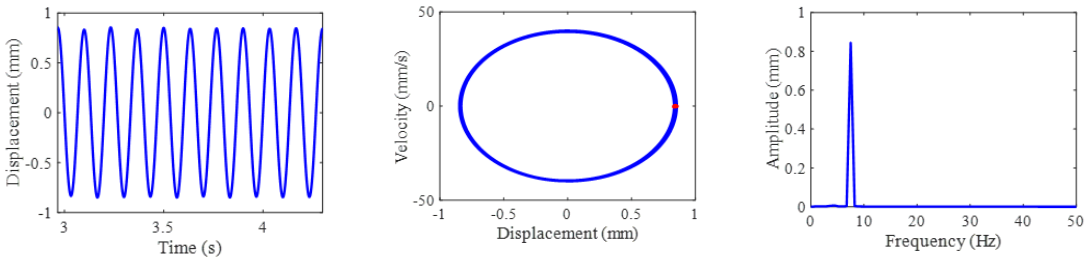

(a) (b) (c)

Figure 12. Theoretical results at 5 m/s²: (a) time history, (b) phase portrait with Poincaré map, (c) amplitude spectrum.

When the excitation amplitude increases to 10.5 m/s^2, the system exhibits period-two vibration (Fig. 13). The time history shows two distinct amplitude displacement curves; the phase portrait forms two closed trajectories; Poincaré points concentrate around two isolated locations; and the amplitude spectrum exhibits peaks at ω = 7.5 Hz and its harmonics.

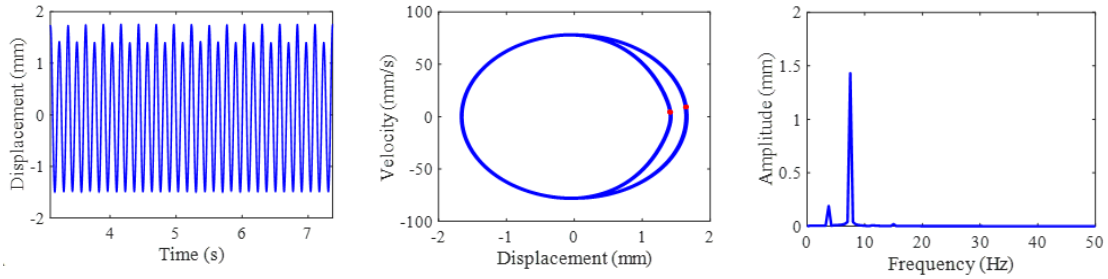

(a) (b) (c)

Figure 13. Theoretical results at 10.5 m/s²: (a) time history, (b) phase portrait with Poincaré map, (c) amplitude spectrum.

At the excitation amplitude of 12.5 m/s^2, the system enters intra-well chaotic vibration (Fig. 14). The plate displays irregular oscillations near the I stable configuration. The time history shows displacements with varying amplitudes; the phase portrait presents multiple irregular trajectories; the Poincaré map shows a scattered distribution; and the amplitude spectrum becomes continuous with peaks relative to periodic motion.

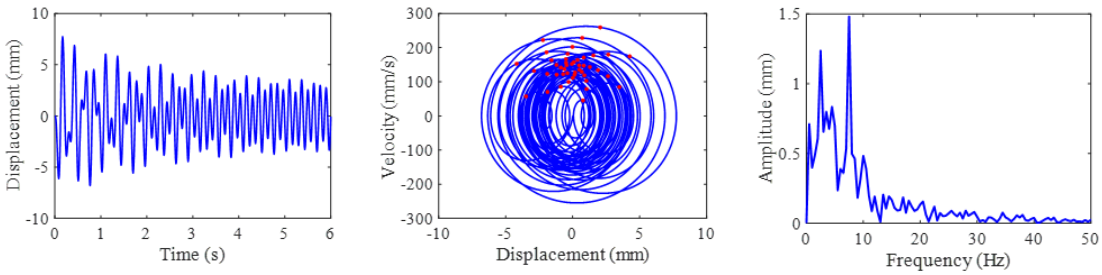

(a) (b) (c)

Figure 14. Theoretical results at 12.5 m/s²: (a) time history, (b) phase portrait with Poincaré map, (c) amplitude spectrum.

At the excitation amplitude of 14 m/s^2, snap-through occurs (Fig. 15), transitioning the system from the I stable configuration to the C stable configuration. The time history displays multiple irregular amplitude curves; the phase portrait shows several irregular trajectories; the Poincaré map is scattered.

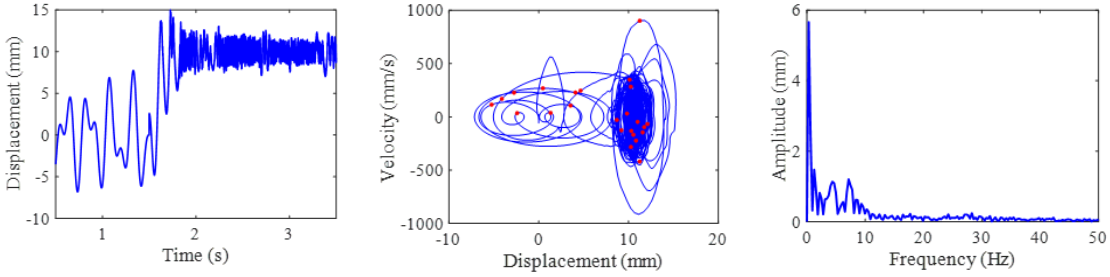

(a) (b) (c)

Figure 15. Theoretical results at 14 m/s²: (a) time history, (b) phase portrait with Poincaré map, (c) amplitude spectrum.

6. Experimental Validation

This section presents experimental results from vibration tests on cantilevered bistable laminates to validate the dynamic model developed in Section 5 and to assess the resonance-based control strategy proposed in Section 7. The measured responses are compared with theoretical predictions, including periodic oscillations, period-doubling bifurcations, chaotic motion, and snap-through, under identical excitation conditions.

After setting up the experimental apparatus and determining the measurement points, frequency-sweep tests are conducted on the four cantilevered bistable composite laminates to systematically investigate their dynamic responses. The experiments maintain a constant

acceleration while gradually varying the excitation frequency at a fixed rate, with both forward and backward sweeps, to obtain the amplitude-frequency curves.

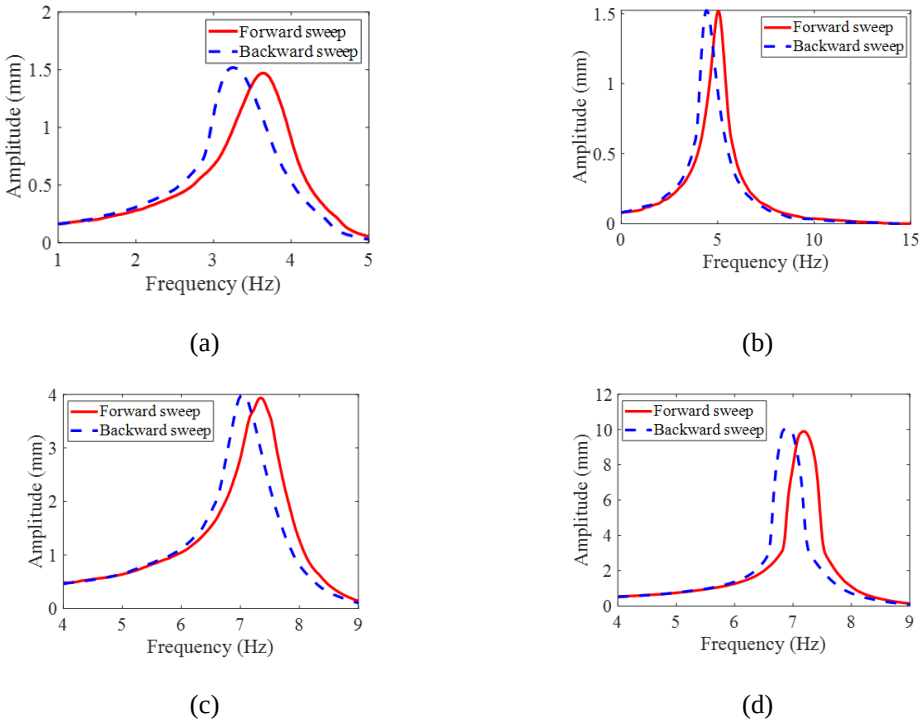

Figure 16. Forward and backward frequency sweep results of the C configuration, (a) 300 × 100 mm, (b)250 × 100 mm, (c)200 × 100 mm, (d) 200 × 80 mm.

Figure 16-17 shows the forward and backward frequency-sweep results of the cantilever bistable composite laminates at an excitation amplitude of 2 m/s². The frequency response curves clearly reflect the nonlinear dynamic behavior and softening effects of plates with different dimensions. As the aspect ratio decreases (the plate becomes shorter and wider), the structural stiffness increases, leading to higher resonant frequencies for both configurations. Meanwhile, the intensity of the nonlinear softening behavior also varies with geometry. For instance, the 200×80 mm specimen exhibits more pronounced nonlinear softening compared to the 300×100 mm specimen, consistent with the model predictions.

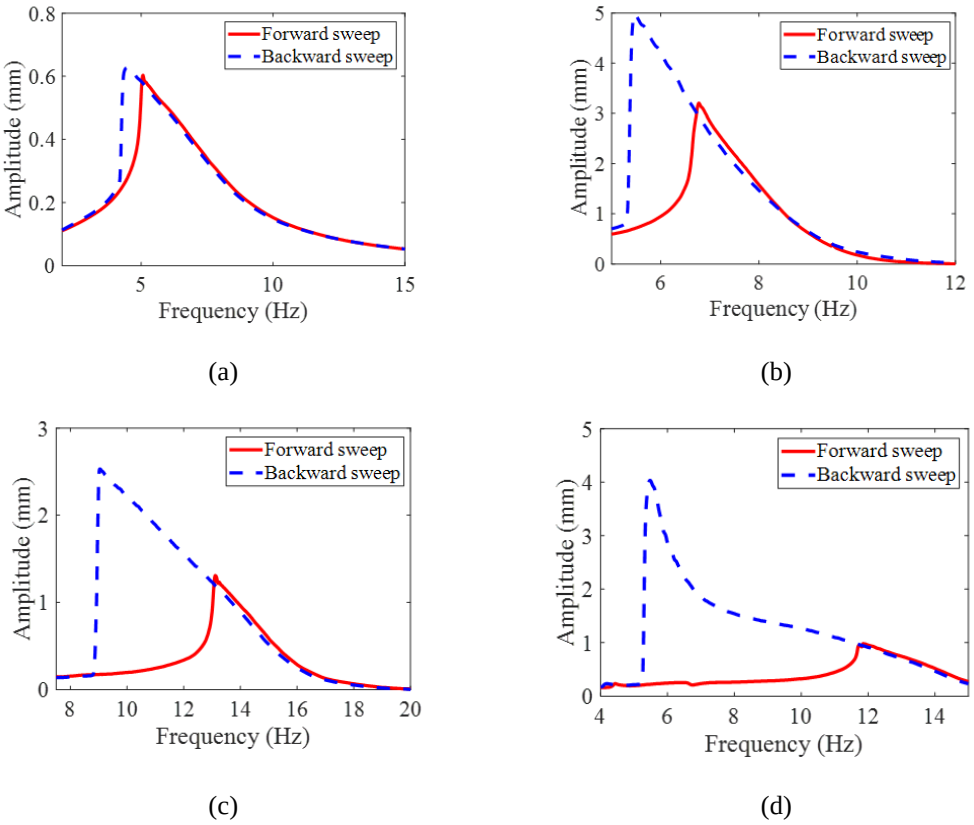

Figure 17. Forward and backward frequency sweep results of the I configuration, (a) 300 × 100 mm, (b)250 × 100 mm, (c)200 × 100 mm, (d) 200 × 80 mm.

In further experiments, the excitation frequency was fixed at 7.5 Hz while the acceleration amplitude was gradually increased in equal increments. The vibration displacement signals collected from numerous tests were processed and compiled into an experimental bifurcation diagram. Figure 18 illustrates the bifurcation evolution of the cantilever bistable composite laminated plate with dimensions of 300 × 100 mm.

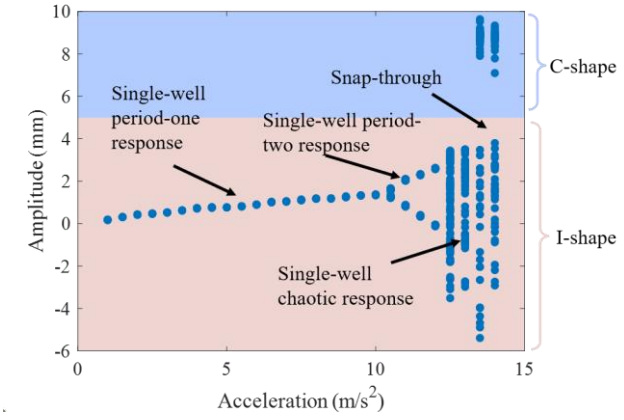

Figure 18. Bifurcation diagram from the experiment at 7.5 Hz.

The results show that when the excitation amplitude reaches 10.5 m/s², the system transitions from single-period vibration to period-two motion. As the excitation amplitude increases to 12.5 m/s², the system evolves from period-two motion to single-well chaotic motion. When the excitation amplitude reached 13.5 m/s², the snap-through occurred, and the structure transitioned from I shape to C shape.

As shown in Figure 19–22, further experiments reveal the typical dynamic responses of the cantilever bistable composite laminated plate under various excitation amplitudes. The structural responses are analyzed in detail through the time histories, phase portraits, Poincaré maps, and frequency spectra. Since a certain loading duration is required for the system to reach the target excitation frequency and amplitude during the experiment, a stable portion of the time history after the transient phase is selected for further analysis, allowing a more accurate characterization of the response type under the given excitation.

At an excitation amplitude of 5 m/s^2, the plate exhibits a single-periodic vibration around the I stable configuration: the time history shows uniform periodic displacements, the phase portrait forms a single closed orbit, the Poincaré map collapses to a single point, and the amplitude spectrum displays a dominant peak only at the driving frequency (Fig. 19).

Increasing the excitation amplitude to 11.5 m/s² leads to period-two motion: two distinct displacement amplitudes appear in the time history, two closed loops emerge in the phase portrait, the Poincaré map splits into two discrete points, and the frequency spectrum exhibits peaks at 3.75 Hz and its multiples (Fig. 20).

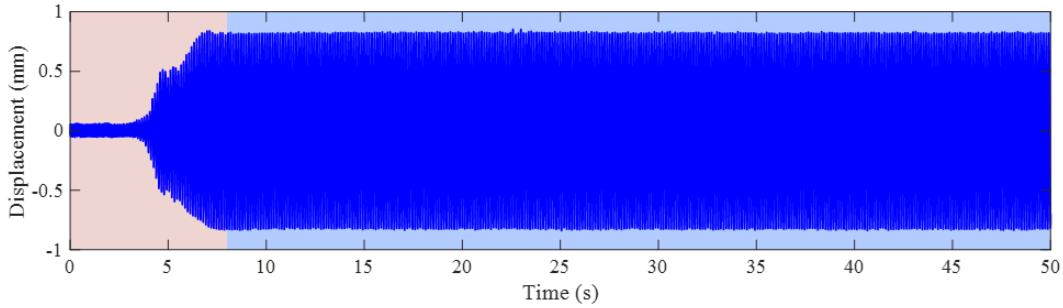

(a)

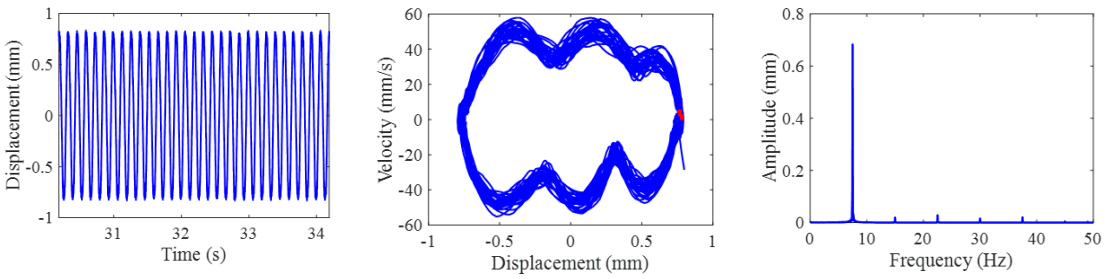

(b) (c) (d)

Figure 19. Experimental results at 5 m/s²: (a) overall time history, (b) selected time history after stabilization, (c) phase portrait with Poincaré map, and (d) amplitude spectrum.

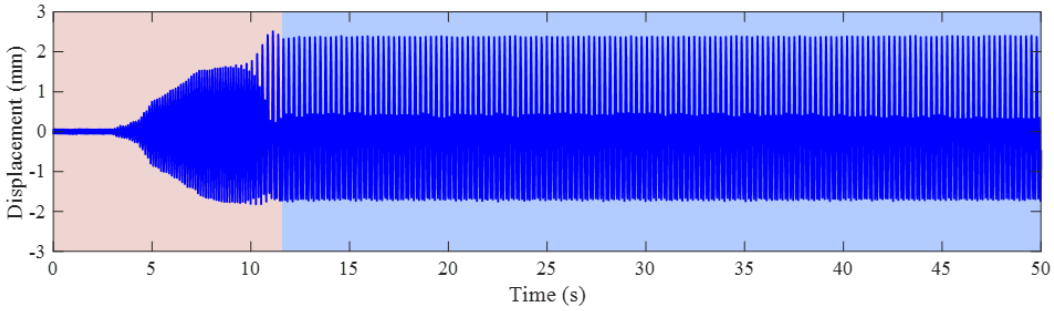

(a)

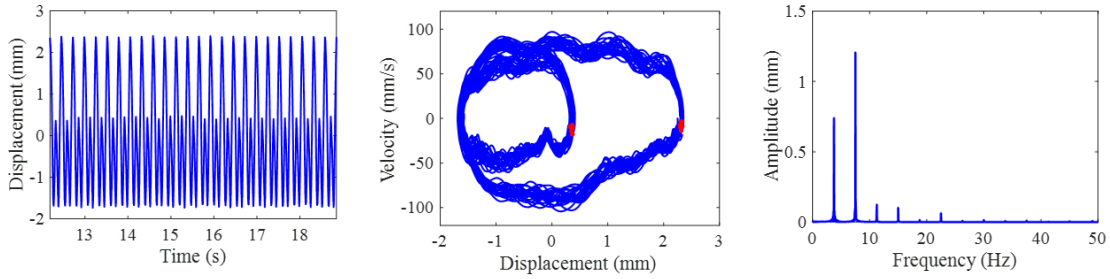

(b) (c) (d)

Figure 20. Experimental results at 11.5 m/s²: (a) overall time history, (b) selected time history after stabilization, (c) phase portrait with Poincaré map, and (d) amplitude spectrum.

Further increasing the excitation amplitude to 12.5 m/s² causes single-well chaotic vibration without configuration switching: irregular displacement waveforms and complex phase trajectories are observed, the Poincaré map displays scattered points, and the amplitude spectrum becomes broadband with continuous components (Fig. 21).

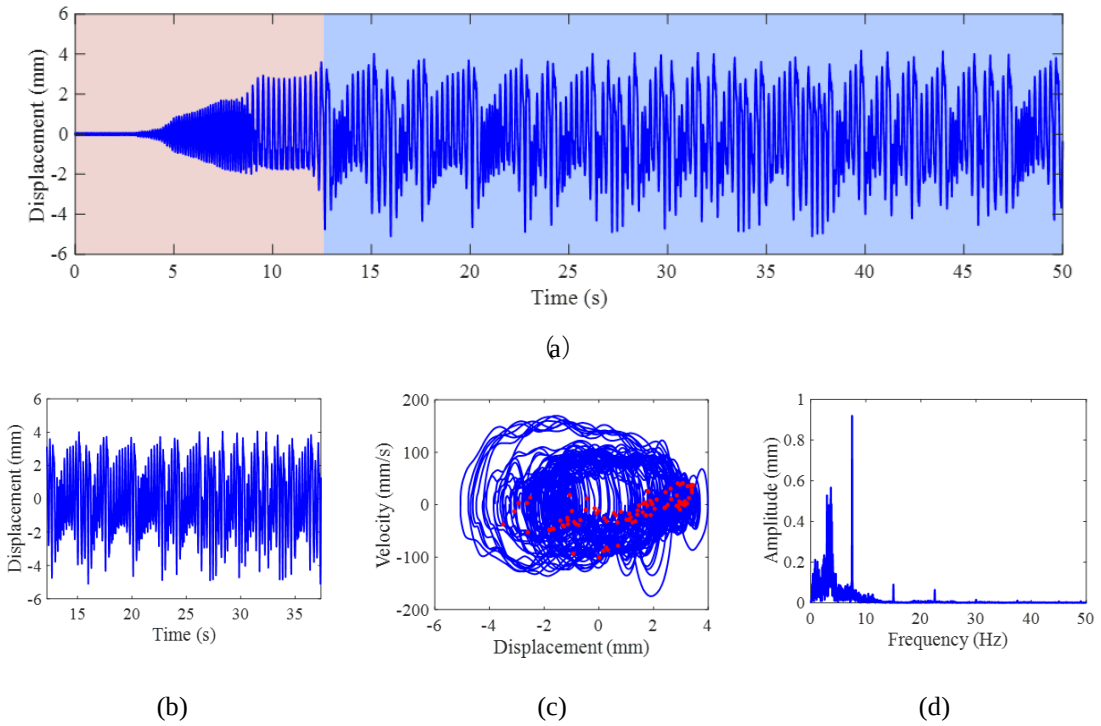

Figure 21. Experimental results at 12.5 m/s²: (a) overall time history, (b) selected time history after stabilization, (c) phase portrait with Poincaré map, and (d) amplitude spectrum.

When the excitation amplitude reaches 13.5 m/s², the system undergoes the dynamic snap-through. Upon completion of the snap-through, the stable configuration of the structure transitions from I-shape to C-shape. Due to the difference in resonant frequencies between the two configurations, the vibration amplitude of the structure significantly reduces (Fig. 22).

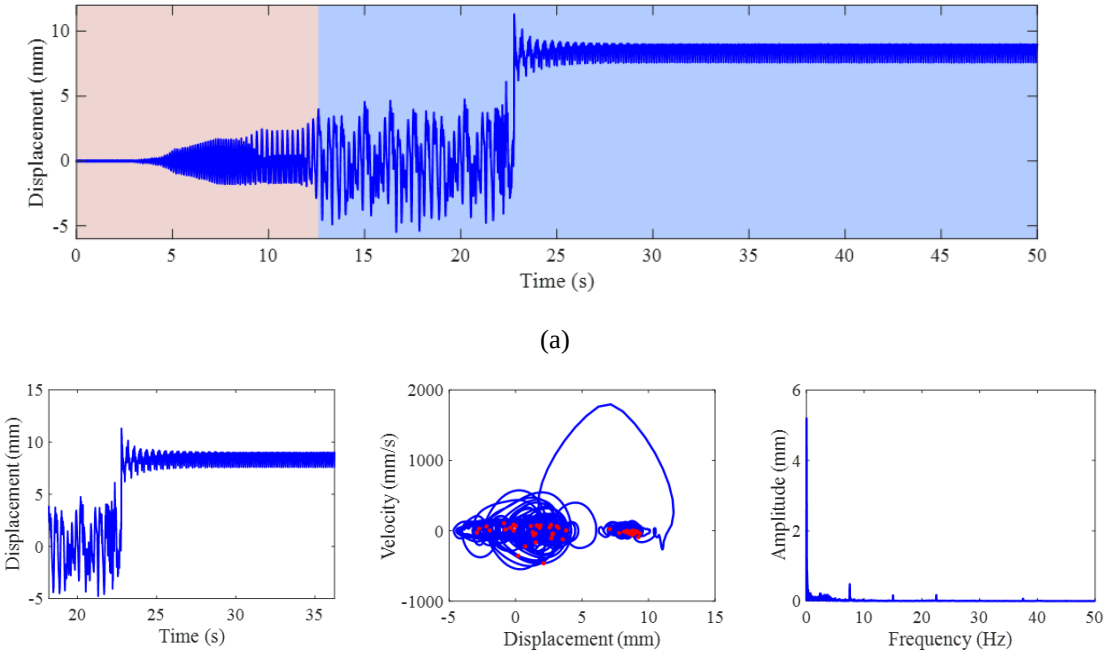

(b) (c) (d)

Figure 22. Experimental results at 13.5 m/s²: (a) overall time history, (b) selected time history after stabilization, (c) phase portrait with Poincaré map, and (d) amplitude spectrum.

These experimental results are in good agreement with the analytical model, confirming the system's transition from single-period motion to period-doubling bifurcations, chaos, and ultimately snap-through behavior.

7. Resonance-Based Control Strategy

7.1 Resonant Actuation Principle

The fundamental idea of the proposed control strategy is to leverage the resonant characteristics of the bistable structure to achieve efficient and rapid configuration transitions. This strategy is an open-loop control method that actively drives the structure from one stable state to the other by injecting energy in a frequency-tuned manner, rather than simply increasing the excitation amplitude. The control process comprises the following key steps:

1.State identification: The current stable configuration of the structure (I shape) is first identified, and the transition to the target configuration (C shape) is defined as the control objective.

2. Resonant frequency selection: Based on the natural frequency of the current stable configuration (I shape) obtained from prior analysis or experiments, an excitation frequency close to that resonance (7.5 Hz) is chosen. This frequency serves as the critical control parameter.

3.Energy injection: A harmonic excitation at the selected frequency is applied via a shaker, with the amplitude gradually increased. The frequency tuning ensures that the input energy is efficiently transferred to the structure, maximizing the vibration amplitude through resonance.

4.Snap-through: As the resonant amplification drives the vibration amplitude beyond the critical snap-through threshold, the structure rapidly transitions from the I shape to the C shape. This dynamic snap-through is the direct result of the control strategy.

5.Excitation cessation and state maintenance: After the snap-through occurs, the external excitation can be turned off if the subsequent dynamic response is not of interest. Owing to

the intrinsic bistability, the structure remains in the new stable configuration (C shape) without requiring further energy input.

This activation strategy ensures that energy is consumed only during the snap-through, capitalizing on the bistability to maintain the new shape passively. Such a feature is critical for practical morphing applications, as it avoids the need for continuous power input and enables sustained shape holding with minimal energy expenditure.

7.2 Experimental Demonstration of Configuration Switching

Figures 23 and 24 present the analytical model and experimental results, respectively, for the bistable plate driven at an excitation frequency of 7.5 Hz, showing the displacement time-history signals and the excitation signal. A rapid switch between stable states was triggered when the displacement reached the critical amplitude from the I stable configuration to the C stable configuration. The excitation amplitude required to trigger the snap-through in the analytical model was 14 m/s², showing close agreement with the experimentally measured value of 13.5 m/s². Following the snap-through, the vibration amplitude quickly diminished, which corresponds to the off-resonance steady-state response of the C Configuration at the driving frequency.

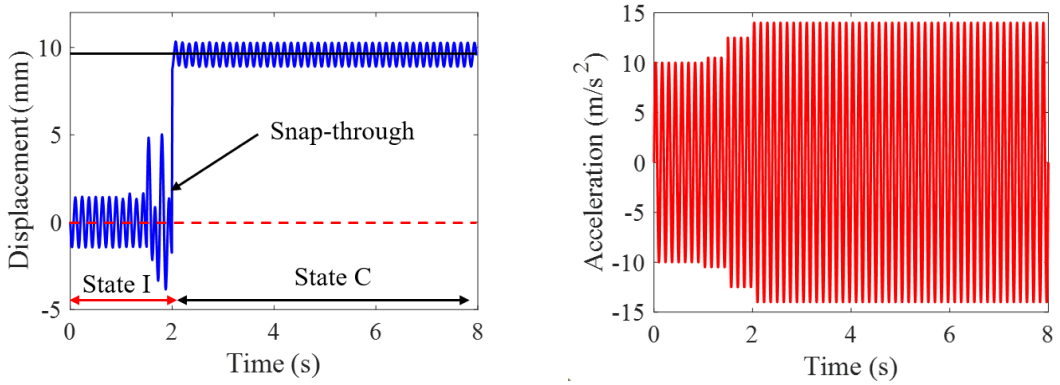

Figure 23. Snap-through of the bistable plate under actuation from theoretical results: (a) time history; (b) excitation signal.

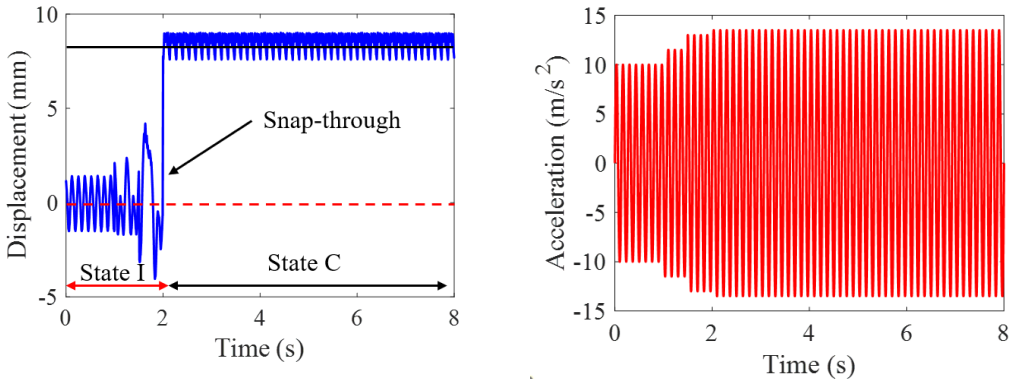

(a) (b)

Figure 24. Snap-through of the bistable plate under actuation from experimental results: (a) time history; (b) excitation signal.

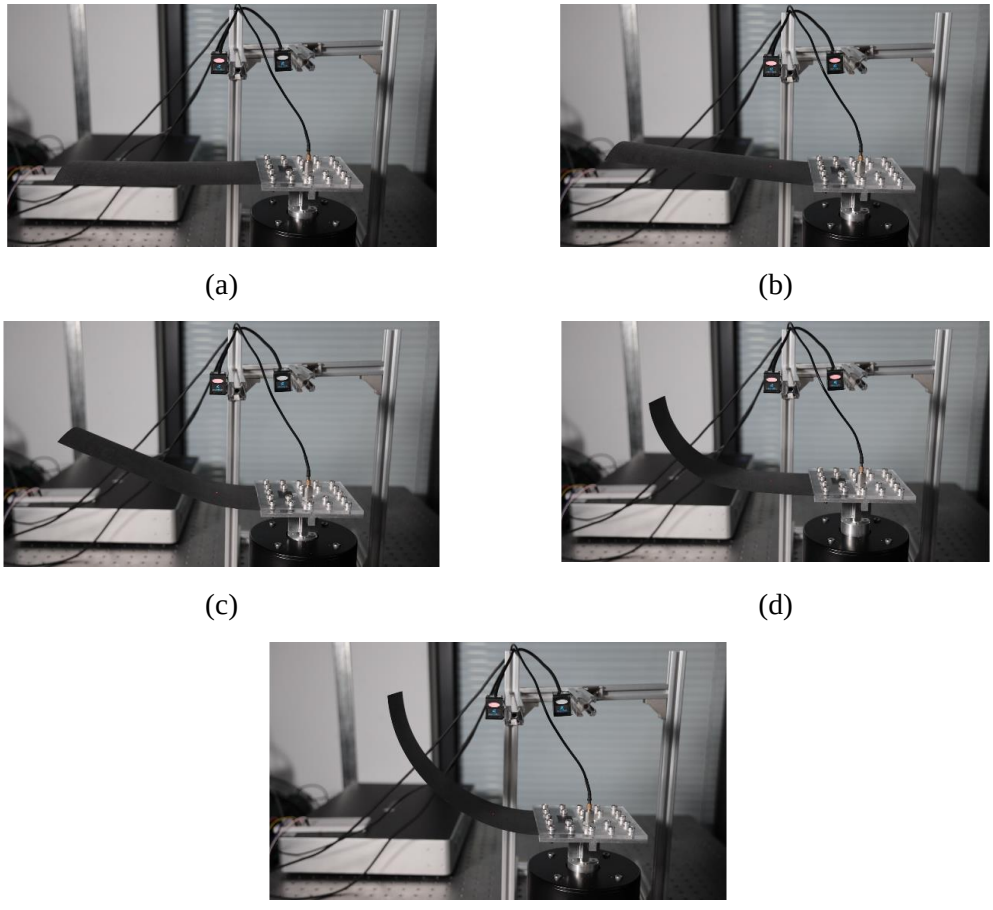

(a) (b)

(c) (d)

(e)

Figure 25. Experimentally captured structural configurations at different time instants after applying the excitation signal: (a) t = 0 s, (b) t = 0.5 s, (c) t = 1.5 s, (d) t = 2 s, (e) t = 3 s.

Through optimization of the specimen's geometry and boundary conditions, a sufficient frequency separation between the two stable configurations was ensured, enabling low-energy and reliable configuration switching.

Figure 25 presents the instantaneous structural configurations of the bistable laminated plate at different moments after the excitation is applied. Figure 25(a)–(e) correspond to t = 0 s, 0.5 s, 1.5 s, 2 s and 3 s, respectively. As the excitation loads, the vibration amplitude gradually increases, and the region of curvature variation extends from the clamped end toward the free end, finally leading to snap-through.

The experimental results confirm the feasibility of this actuation strategy for bistable laminated cantilever plates, providing a practical foundation for future full-shape morphing control of more complex bistable structures such as morphing wings.

8.Conclusions

This study systematically investigates the nonlinear dynamic characteristics of cantilevered bistable composite laminates under different external excitation through theoretical model and vibration experiments, and proposes a control strategy to drive snap-through. The main conclusions are as follows:

1.Through theoretical model and experiments, the nonlinear dynamics of cantilevered bistable laminates under different excitation amplitudes were analyzed. The results show that as the excitation amplitude increases, the dynamic behavior of the system transitions from periodic motion to chaotic motion, and finally lead to snap-through. The experimental results are generally consistent with the analytical model, validating the effectiveness of the model. It is noteworthy that structural dynamic snap-through is often accompanied by chaotic vibrations, which may create favorable conditions for the occurrence of snap-through.

2. Based on the nonlinear dynamic characteristics of cantilevered bistable composite laminates, a resonance-driven control strategy is proposed to achieve efficient and reliable configuration switching. This strategy significantly amplifies the vibration amplitude of cantilevered bistable laminates through resonance, rapidly driving the structure to reach critical amplitude and inducing configuration transition.

3. After snap-through completion, due to the different resonant frequencies of the two stable configurations, the vibration amplitude of the laminate rapidly decreases, thereby avoiding excessive oscillations. This strategy achieves efficient configuration control of cantilevered bistable laminates, enhances deformation capability, and provides a practical method for deformation control of complex bistable structures in engineering applications.

Reference

Arrieta, A.F., Bilgen, O., Friswell, M.I., Ermanni, P., 2012. Passive load alleviation bi-stable morphing concept. AIP Advances 2, 032118.

Arrieta, A.F., Bilgen, O., Friswell, M.I., Ermanni, P., 2013. Modelling and configuration control of wing-shaped bi-stable piezoelectric composites under aerodynamic loads. Aerospace Science and Technology 29, 453-461.

Arrieta, A.F., Kuder, I.K., Rist, M., Waeber, T., Ermanni, P., 2014. Passive load alleviation aerofoil concept with variable stiffness multi-stable composites. Composite Structures 116, 235-242.

Arrieta, A.F., Neild, S.A., Wagg, D.J., 2009. Nonlinear dynamic response and modeling of a bi-stable composite plate for applications to adaptive structures. Nonlinear Dynamics 58, 259-272.

Arrieta, A.F., Wagg, D.J., Neild, S.A., 2011. Dynamic Snap-through for Morphing of Bi-stable Composite Plates. Journal of Intelligent Material Systems and Structures 22, 103-112.

Barbarino, S., Bilgen, O., Ajaj, R., Friswell, M.I., Inman, D., 2011. A Review of Morphing Aircraft. Journal of Intelligent Material Systems and Structures 22, 823-877.

Betts, D.N., Kim, H.A., Bowen, C.R., 2012. Optimization of Stiffness Characteristics for the Design of Bistable Composite Laminates. AIAA Journal 50, 2211-2218.

Bilgen, O., Arrieta, A.F., Friswell, M.I., Hagedorn, P., 2013. Dynamic control of a bistable wing under aerodynamic loading. Smart Materials and Structures 22, 025020.

Boddapati, K., Arrieta, A.F., 2021. Design of Bistable Laminates With Low Aspect Ratio, ASME 2021 Conference on Smart Materials, Adaptive Structures and Intelligent Systems, p. V001T005A017.

Boddapati, K., Boston, D.M., Rivas-Padilla, J.R., Arrieta, A.F., 2023. Aero-Structural Response of a Slitted Bistable Laminate, ASME 2023 Conference on Smart Materials, Adaptive Structures and Intelligent Systems, p. V001T004A004.

Boddapati, K., Osorio, J.C., Arrieta, A.F., 2024. On maintaining bistability of prestressed laminates after clamping. Composite Structures 344, 118278.

Bolsman, C.T., Goosen, J.F.L., van Keulen, F., 2009. Design Overview of a Resonant Wing Actuation Mechanism for Application in Flapping Wing MAVs. International Journal of Micro Air Vehicles 1, 263-272.

Brampton, C.J., Betts, D.N., Bowen, C.R., Kim, H.A., 2013. Sensitivity of bistable laminates to uncertainties in material properties, geometry and environmental conditions. Composite Structures 102, 276-286.

Brunetti, M., Favata, A., Vidoli, S., 2020. Enhanced models for the nonlinear bending of planar rods: localization phenomena and multistability. Proceedings of the Royal Society A: Mathematical, Physical and Engineering Sciences 476, 20200455.

Brunetti, M., Kloda, L., Romeo, F., Warminski, J., 2018a. Multistable cantilever shells: Analytical prediction, numerical simulation and experimental validation. Composites Science and Technology 165, 397-410.

Brunetti, M., Mitura, A., Romeo, F., Warminski, J., 2022. Nonlinear dynamics of bistable composite cantilever shells: An experimental and modelling study. Journal of Sound and Vibration 526, 116779.

Brunetti, M., Vidoli, S., Vincenti, A., 2018b. Bistability of orthotropic shells with clamped boundary conditions: An analysis by the polar method. Composite Structures 194, 388-397.

Brunetti, M., Vincenti, A., Vidoli, S., 2016. A class of morphing shell structures satisfying clamped boundary conditions. International Journal of Solids and Structures 82, 47-55.

Dano, M.-L., Hyer, M.W., 1998. Thermally-induced deformation behavior of unsymmetric laminates. International Journal of Solids and Structures 35, 2101-2120.

Dano, M.L., Hyer, M.W., 2002. Snap-through of unsymmetric fiber-reinforced composite laminates. International Journal of Solids and Structures 39, 175-198.

Daynes, S., Nall, S.J., Weaver, P.M., Potter, K.D., Margaris, P., Mellor, P.H., 2010. Bistable Composite Flap for an Airfoil. Journal of Aircraft 47, 334-338.

Daynes, S., Weaver, P., Trevarthen, J.A., 2011. A Morphing Composite Air Inlet with Multiple Stable Shapes. Journal of Intelligent Material Systems and Structures 22, 961-973.

Diaconu, C.G., Weaver, P.M., Mattioni, F., 2008. Concepts for morphing airfoil sections using bi-stable laminated composite structures. Thin-Walled Structures 46, 689-701.

Hyer, M.W., 1981. Some Observations on the Cured Shape of Thin Unsymmetric Laminates. Journal of Composite Materials 15, 175-194.

Kakogawa, A., Jeon, S., Ma, S., 2018. Stiffness Design of a Resonance-Based Planar Snake Robot With Parallel Elastic Actuators. IEEE Robotics and Automation Letters 3, 1284-1291.

Kim, J.S., Wang, K.W., Smith, E.C., 2008. Synthesis and control of piezoelectric resonant actuation systems with buckling-beam motion amplifier. AIAA journal 46, 787-791.

Kim, S.W., Koh, J.S., Cho, M., Cho, K.J., 2010. Towards a bio-mimetic flytrap robot based on a snap-through mechanism, 2010 3rd IEEE RAS & EMBS International Conference on Biomedical Robotics and Biomechatronics, pp. 534-539.

Kuder, I.K., Arrieta, A.F., Rist, M., Ermanni, P., 2016. Aeroelastic response of a selectively compliant morphing aerofoil featuring integrated variable stiffness bi-stable laminates. Journal of Intelligent Material Systems and Structures 27, 1949-1966.

Liu, Y., Huang, K., Zhang, J., 2026. The resonant actuation and optimization design of piezoelectrically actuated bistable composite laminates. Thin-Walled Structures 219, 114265.

Liu, Y., Zhang, J., Pan, D., Wu, Z., Wang, Q., 2023. Resonant Actuation Based on Dynamic Characteristics of Bistable Laminates, Machines, p. 318.

Mattioni, F., Weaver, P.M., Friswell, M.I., 2009. Multistable composite plates with piecewise variation of lay-up in the planform. International Journal of Solids and Structures 46, 151-164.

Mattioni, F., Weaver, P.M., Potter, K.D., Friswell, M.I., 2008. Analysis of thermally induced multistable composites. International Journal of Solids and Structures 45, 657-675.

Molinari, G., Arrieta, A.F., Guillaume, M., Ermanni, P., 2016. Aerostructural Performance of Distributed Compliance Morphing Wings: Wind Tunnel and Flight Testing. AIAA Journal 54, 3859-3871.

Nicassio, F., Scarselli, G., Pinto, F., Ciampa, F., Iervolino, O., Meo, M., 2018. Low energy actuation technique of bistable composites for aircraft morphing. Aerospace Science and Technology 75, 35-46.

Pirrera, A., Avitabile, D., Weaver, P.M., 2010. Bistable plates for morphing structures: A refined analytical approach with high-order polynomials. International Journal of Solids and Structures 47, 3412-3425.
Potter, K., Weaver, P., Seman, A.A., Shah, S., 2007. Phenomena in the bifurcation of unsymmetric composite plates. Composites Part A: Applied Science and Manufacturing 38, 100-106.
Reich, G., Sanders, B., 2007. Introduction to Morphing Aircraft Research. Journal of Aircraft 44, 1059-1059.
Sanders, B., Eastep, F.E., Forster, E., 2003. Aerodynamic and Aeroelastic Characteristics of Wings with Conformal Control Surfaces for Morphing Aircraft. Journal of Aircraft 40, 94-99.
Schioler, T., Pellegrino, S., 2008. A bistable structural element. ARCHIVE Proceedings of the Institution of Mechanical Engineers Part C Journal of Mechanical Engineering Science 1989-1996 (vols 203-210) 222.
Stanewsky, E., 2000. Aerodynamic benefits of adaptive wing technology. Aerospace Science and Technology 4, 439-452.
Taghipour, J., Zhang, J., Shaw, A.D., Friswell, M.I., Gu, H., Wang, C., 2022. Resonant passive energy balancing of morphing helicopter blades with bend–twist coupling. Nonlinear Dynamics 107, 617-639.
Wang, J., Zhang, P., Li, X., Cao, D., 2025a. Nonlinear dynamics of bistable rectangular asymmetric composite laminate: Theory, simulation and experiment. Applied Mathematical Modelling 146, 116183.
Wang, Z.Q., Yang, S.W., Hao, Y.X., Zhang, W., Ma, W.S., Niu, Y., 2025b. High-dimensional nonlinear flutter suppression of variable thickness porous sandwich conical shells based on nonlinear energy sink. Journal of Sound and Vibration 595, 118731.
Wu, M.Q., Zhang, W., Niu, Y., 2021. Experimental and numerical studies on nonlinear vibrations and dynamic snap-through phenomena of bistable asymmetric composite laminated shallow shell under center foundation excitation. European Journal of Mechanics - A/Solids 89, 104303.
Wu, Z., Li, H., Chen, Y., 2020. An improved model for unsymmetric plates. Composite Structures 252, 112622.
Yao, M., Wang, S., Niu, Y., Wu, Q., Wang, C., 2024. Vibration characteristics of pre-twisted rotating Ti-SiC composite airfoil blade. Applied Mathematical Modelling 128, 392-409.
Zhang, J., Shaw, A.D., Wang, C., Gu, H., Amoozgar, M., Friswell, M.I., 2022. Resonant passive energy balancing for a morphing helicopter blade. Aerospace Science and Technology 128, 107786.
Zhang, J., Wu, Z., Zhang, C., Hao, L., Nie, R., Qiu, J., 2019. Nonlinear dynamics of shape memory alloys actuated bistable beams. Smart Materials and Structures 28, 055009.
Zhang, P., Li, X., Wang, J., 2025. Nonlinear effect on stable state and snap-through bistability of square composite laminate. European Journal of Mechanics - A/Solids 109, 105431.
Zheng, Y., Zhang, W., Liu, T., 2021. Coexistence of double-parameter nonlinear dynamics and metastable chaos for bistable asymmetric composite laminated square panel under combined external and parametric excitations. Nonlinear Dynamics 104, 2071-2098.